

## Article

# Highly Sensitive Temperature Sensors Resulting from the Luminescent Behavior of Sm<sup>3+</sup>-Doped Ba<sub>2</sub>MgMoO<sub>6</sub> High-Symmetry Double-Perovskite Molybdate Phosphors

Natalia Miniajluk-Gaweł \*, Bartosz Bondzior , Maciej Ptak  and Przemysław Jacek Dereń \* 

Institute of Low Temperature and Structure Research, Polish Academy of Science, Okolna 2, 50-422 Wrocław, Poland; b.bondzior@intibs.pl (B.B.); m.ptak@intibs.pl (M.P.)

\* Correspondence: n.miniajluk@intibs.pl (N.M.-G.); p.deren@intibs.pl (P.J.D.)

**Abstract:** We present double-perovskite molybdate with the formula of Ba<sub>2</sub>MgMoO<sub>6</sub> doped with Sm<sup>3+</sup> ions as a potential red phosphor to improve the color characteristics of white-light-emitting diodes (wLEDs). The new orange–red phosphor was synthesized using the co-precipitation (CP) method, and then its structural and spectroscopic properties were determined. Red emission at 642.6 nm dominates, which results from the electric dipole (ED) transition of the <sup>4</sup>G<sub>5/2</sub> → <sup>6</sup>H<sub>9/2</sub> type, and the materials are characterized by short luminescence decay times. BMM:Sm<sup>3+</sup> is, to our best knowledge, the clearest example of dominant red emission of Sm<sup>3+</sup> resulting from the location of the dopant in octahedral sites of high-symmetry cubic structure. In the sample containing 0.1% Sm<sup>3+</sup>, Sm<sup>3+</sup> ions are located in both Mg<sup>2+</sup> and Ba<sup>2+</sup> sites, while at higher concentrations the Ba<sup>2+</sup> site is less preferable for doping, as a result of which the emission becomes more uniform and single-site. The relative sensitivity calculated from FIR has a maximum of 2.7% K<sup>−1</sup> at −30 °C and another local maximum of 1.6% K<sup>−1</sup> at 75 °C. Such value is, to the best of our knowledge, one of the highest achieved for luminescent thermometry performed using only Sm<sup>3+</sup> ions. To sum up, the obtained materials are good candidates as red phosphor to improve the color characteristics of wLEDs, obtaining a color-rendering index (CRI) of 91 and coordinated color temperature (CCT) of 2943 K, constituting a warm white emission. In addition to this, a promising precedent for temperature sensing using high-symmetry perovskite materials is the high sensitivity achieved, which results from the high symmetry of the BMM host.

**Keywords:** double-perovskite; molybdate phosphors; high symmetry; WLED; optical thermometer



**Citation:** Miniajluk-Gaweł, N.; Bondzior, B.; Ptak, M.; Dereń, P.J. Highly Sensitive Temperature Sensors Resulting from the Luminescent Behavior of Sm<sup>3+</sup>-Doped Ba<sub>2</sub>MgMoO<sub>6</sub> High-Symmetry Double-Perovskite Molybdate Phosphors. *Materials* **2024**, *17*, 1897. <https://doi.org/10.3390/ma17081897>

Academic Editors: Ruihao Chen and Zhou Xing

Received: 27 March 2024

Revised: 15 April 2024

Accepted: 17 April 2024

Published: 19 April 2024



**Copyright:** © 2024 by the authors. Licensee MDPI, Basel, Switzerland. This article is an open access article distributed under the terms and conditions of the Creative Commons Attribution (CC BY) license (<https://creativecommons.org/licenses/by/4.0/>).

## 1. Introduction

Molybdates are materials based on an oxyanion group Mo<sub>x</sub>O<sub>y</sub>, finding applications in fields like paramagnetic materials [1], catalysts [2], and optical materials [3,4]. Recently, the interest of the research community has grown as the double-perovskite materials were seen as promising due to their highly symmetrical structure, and molybdates are one of the most popular types of inorganic materials found to exhibit the double-perovskite structure described with the formula A<sub>2</sub>BB'O<sub>6</sub>, where A sites are occupied by alkaline metals or lanthanides, while positions B and B' are reserved for transition metal ions. This arrangement creates a more complex and layered crystal lattice compared to the simple perovskite structure. Double-perovskite molybdates exhibit high thermal and chemical stability, and suitability for the luminescent dopants [5], which set that class of materials apart from other double-perovskites, such as halides.

Examples of these materials include Sr<sub>2</sub>FeMoO<sub>6</sub>, known for its colossal magnetoresistance (CMR) effect, which makes it a promising candidate for applications in spintronics and magnetic sensors [6], and Ba<sub>2</sub>PrMoO<sub>6</sub>, explored for its photocatalytic and photocurrent properties, making it relevant for applications in solar energy conversion and water splitting [7].

The research on the luminescence properties of double-perovskite molybdates is limited, with most of the published articles being focused on  $\text{Eu}^{3+}$  luminescence [5,8–10]. It is apparent that the rare earth dopants tend to locate themselves in highly symmetrical octahedral  $\text{MgO}_6$  sites, which are credited for their unique luminescence properties in the form of almost-monochromatic emission spectra [8,9]. This work concerns the  $\text{Ba}_2\text{MgMoO}_6$  double-perovskite, and so far, only three publications [9,11,12] have been published on  $\text{Eu}^{3+}$  doping. It should be emphasized that this is the first work that describes the physico-chemical properties of this matrix doped with  $\text{Sm}^{3+}$  ions.

Mo-based double-perovskite phosphors are of great interest due to reliable, lasting and stable emission, easy fabrication, low cost, high durability, and strong absorption in the NUV region [11–13]. The  $\text{Sm}^{3+}$  ion was used as an activator of phosphors because these ions have a rich structure of energy levels and can transfer electrons through the 4f-4f transitions. This makes  $\text{Sm}^{3+}$ -doped phosphors generally exhibit multiple absorption peaks in the range of 220–550 nm, and thus they can be excited effectively using a near-UV or blue LED chip. These phosphors emit red–orange light in the visible range with four narrow emission bands, thanks to the characteristic transitions  $^4\text{G}_{5/2} \rightarrow ^6\text{H}_J$  ( $J = 5/2, 7/2, 9/2$  and  $11/2$ ) [14,15].

Temperature is one of the most important physical parameters, so its precise measurement is extremely important. Non-contact luminescent thermometers, compared to traditional contact thermometers, offer many advantages such as non-invasive measurement, fast response, high sensitivity, ability to be used in rapidly changing conditions, and strong electromagnetic fields. The most commonly used temperature reading is based on the relative intensity ratio of two different emission bands, because this method minimizes the influence of disturbing external factors [9,16]. It turned out that the material we proposed, apart from being an excellent material for improving the quality of WLED lighting, can also be successfully used as a highly sensitive optical thermometer, which results directly from the high symmetry. The current state of the research on molybdate phosphors for temperature sensors is not extensive and mainly concerns alkaline earth molybdates [17–19]. However, there is no information about double-perovskites, so this work is very valuable and provides new information regarding non-contact thermometry.

In this paper, double-perovskite molybdate with the formula  $\text{Ba}_2\text{MgMoO}_6$  is studied as a host for  $\text{Sm}^{3+}$  and as a potential red phosphor to improve the color characteristics of wLEDs. For  $\text{Sm}^{3+}$ -doped materials for wLED, the main challenge is to obtain mostly red emission at ~645 nm at the expense of the yellow (570 nm), orange (600 nm), and NIR (710 nm) emissions [20]. We synthesized a novel orange–red phosphor using the co-precipitation method, and then investigated the luminescence properties of these phosphors as representative materials.  $\text{Ba}_2\text{MgMoO}_6$  double-perovskite as a host for  $\text{Sm}^{3+}$  ions has the advantage of high site symmetry and host-sensitization in the near-UV region. Additionally, the obtained temperature measurements results showed that  $\text{Ba}_2\text{MgMoO}_6:\text{Sm}^{3+}$  double-perovskite has a great potential for applications in non-contact optical thermometry.

### 1.1. Experimental

#### Samples Preparation

The co-precipitation synthesis method was used to synthesize a series of  $\text{Sm}^{3+}$ -doped  $\text{Ba}_2\text{MgMoO}_6$  (BMM) double-perovskite samples, described using the formula  $\text{Ba}_2\text{Mg}_{1-x}\text{Sm}_x\text{MoO}_6$  ( $x = 0.1$ –1%).

$\text{Ba}(\text{CH}_3\text{COO})_2$  (Alfa Aesar (Ward Hill, MA, USA), 99%),  $\text{Mg}(\text{CH}_3\text{COO})_2 \cdot 4\text{H}_2\text{O}$  (Alfa Aesar, 99.95%),  $(\text{NH}_4)_6\text{Mo}_7\text{O}_{24} \cdot 4\text{H}_2\text{O}$  (AMT) (Sigma–Aldrich (St. Louis, MO, USA), 99.99%),  $\text{Sm}(\text{NO}_3)_3$  (Alfa Aesar, 99.9%) were used as starting materials in the co-precipitation method.  $\text{Li}_2\text{CO}_3$  (Alfa Aesar, 99.998%) was applied to charge compensation in a ratio of 1:1, based on the amount of dopant ions. To compensate for the evaporation of magnesium ions during the sintering process, a 20% excess of magnesium ions was applied. Firstly, the stoichiometric amounts of precursors were dissolved separately in distilled water. Next, a white precipitate was formed immediately after the first droplet of AMT solution was

added slowly (2 mL/min) under stirring at 200 rpm, 25 °C to the remaining clear solution. The water was evaporated and the precipitate was dried by heating at 80 °C for 20 h and then pre-sintering at 600 °C for 12 h. The final annealing was carried out at 1150 °C for 6 h with a constant heating rate of 3 °C/min using corundum crucible. After each step, the obtained products were ground for 15 min.

### 1.2. Research Techniques

X-ray diffraction (XRD) patterns were recorded with X'Pert ProPANalytical X-ray diffractometer (Malvern, UK), working in the reflection geometry, using CuK $\alpha$  radiation ( $\lambda = 1.54056 \text{ \AA}$ ). The data were collected in a  $2\Theta$  range from 10° to 90° with a step of 0.026°.

Raman spectra were measured using a Renishaw inVia spectrometer (Middlewich, UK) equipped with a confocal optical microscope and a diode laser operating at 830 nm.

A scanning electron microscope (FEI NOVA NanoSEM 230 (Eindhoven, The Netherlands), equipped with EDAX Genesis XM4 detector (Eindhoven, The Netherlands)) was used to characterize the morphology and chemical composition of the samples. The SEM images were recorded with an accelerating voltage of 5 kV.

Emission spectra, excitation spectra, and decay curves were measured using an FLS1000 Edinburgh Instruments (Edinburgh, Scotland) spectrophotometer in a Czerny–Turner configuration with VIS and NIR at room temperature.

The diffuse reflection spectrum was recorded using a Varian Cary 5E UV/VIS-NIR spectrophotometer (Varian Incorporation, Palo Alto, CA, USA).

The emission spectrum as a function of temperature was measured using the Linkam THMS600 (Salfords, UK) stage, which has both heating and cooling functions and Hamamatsu R928 photomultiplier (Hamamatsu, Japan). The measurement was carried out in the range from  $-193 \text{ °C}$  to  $150 \text{ °C}$  with a constant step of  $20 \text{ °C}$ .

## 2. Results and Discussion

### 2.1. Structural Properties

Figure 1a shows X-ray diffractograms of molybdate materials synthesized using the co-precipitation method, along with the visualization of the structure. There is no standard pattern for the structure of BMM, but according to what was written in the previous publication [9], the structure of this material matches well with the ICDD 070-2023 pattern of Ba<sub>2</sub>MgWO<sub>6</sub> (see Figure 1a). It was possible to obtain practically single-phase materials with a small amount of an additional phase of BaMoO<sub>4</sub> ICDD 43-0646 (less than 1%), the presence of which does not in any way affect the physicochemical properties of the obtained materials. It can be seen that, as the Sm<sup>3+</sup> concentration increases, the diffractograms shift towards lower theta angles (Figure 1b). This means that, as the amount of Sm<sup>3+</sup> increases, the lattice constants increase because the smaller ion in the host (Mg<sup>2+</sup>, IR = 86 pm) is replaced by a larger one (Sm<sup>3+</sup>, IR = 109 pm). The obtained materials have a cubic structure, crystallizing in the *Fm* $\bar{3}$ *m* space group (Figure 1c), and are characterized by the following cell parameters:  $a = 8.1120 \text{ \AA}$ , unit cell volume  $V = 533.81 \text{ \AA}^3$  and  $Z = 4$ .

In the SEM image (Figure 1d), one can notice that the obtained material consists of crystallites of undefined shapes: oval with rounded edges. We determined the average crystallite sizes in the ImageJ 1.51j8 program, and they are 0.62  $\mu\text{m}$ . The Supplementary Materials contains a histogram of the average crystal size, determined on the basis of 100 crystallites (Figure S1).

To further check the quality of the samples, Raman spectra were collected (see Figure 1e). The spectrum presents two narrow bands near 126 (F<sub>2g</sub>) and 438 cm<sup>-1</sup> (F<sub>2g</sub>) as well as broader Raman peaks near 780 cm<sup>-1</sup> (A<sub>1g</sub>), which is in good agreement with the previously reported experimental and theoretical data for molybdates and tungstates having double-perovskite architecture [21,22]. The cubic *Fm* $\bar{3}$ *m* structure exhibits only four optical phonons (A<sub>1g</sub> + E<sub>g</sub> + 2F<sub>2g</sub>), but the Raman band corresponding to the E<sub>g</sub> mode is usually too weak to be detected [22,23].

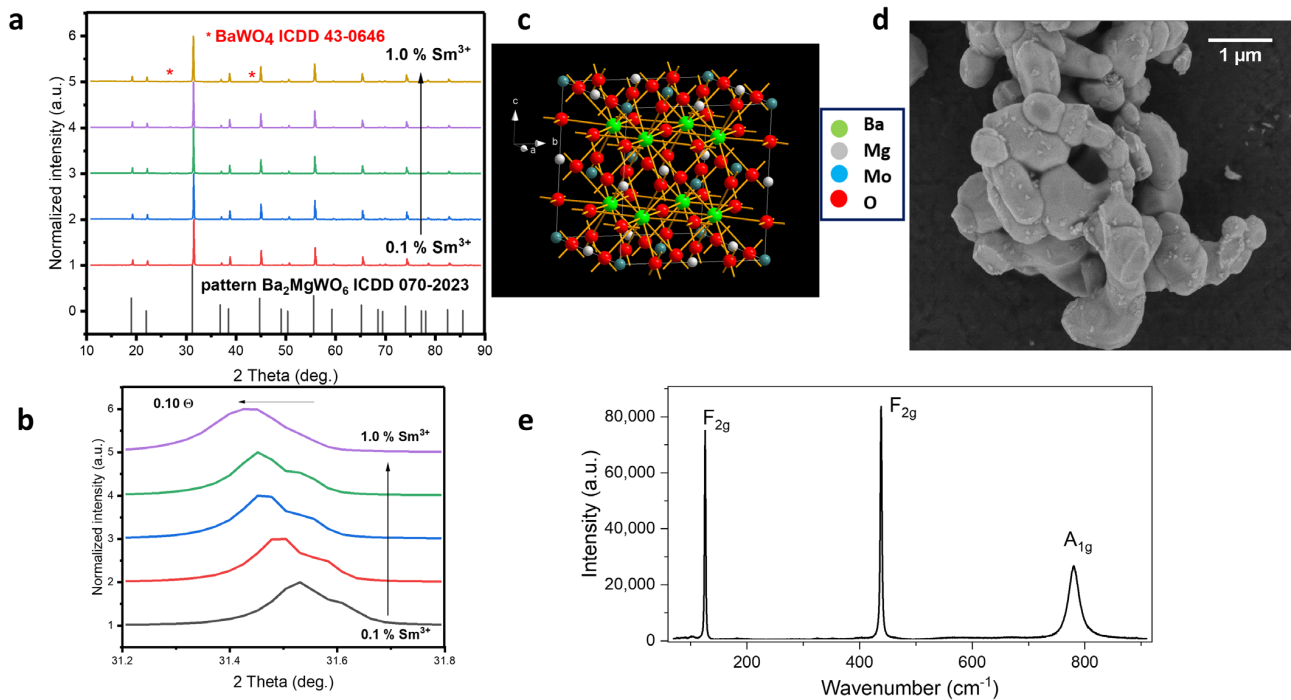


**Figure 1.** (a) XRD results of the studied dopable-perovskite BMM doped with  $\text{Sm}^{3+}$ , (b) XRD lines shift. (c) Unit cell of BMM with the space group  $Fm\bar{3}m$  (d) SEM image and (e) Raman spectra of the BMM: 1.0%  $\text{Sm}^{3+}$ .

## 2.2. Spectroscopic Properties

The absorption spectra of BMM: $\text{Sm}^{3+}$  exhibit absorption peaks in the near infrared, where the lower-lying levels of  $\text{Sm}^{3+}$  are located (Figure 2a inset). These absorption lines are primarily due to  ${}^6\text{H}_{5/2} \rightarrow {}^6\text{F}_J$  ( $J = 1/2, \dots, 11/2$ ) transitions.

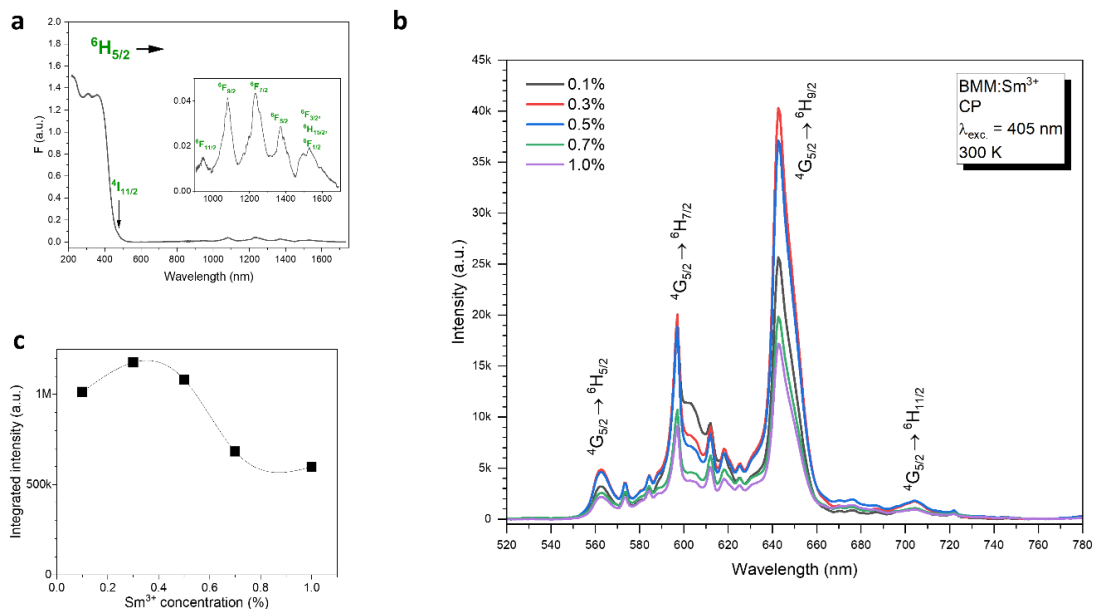


**Figure 2.** (a) Absorption spectra of the BMM: 1.0%  $\text{Sm}^{3+}$ , (b) emission spectra, (c) integral emission intensity. The line in (c) serves only to guide the eye.

The emission spectra of the BMM: $\text{Sm}^{3+}$  (Figure 2b) exhibit four emission peaks resulting from the  ${}^4\text{G}_{5/2} \rightarrow {}^6\text{H}_J$  ( $J = 5/2, \dots, 11/2$ ) transitions, characteristic of  $\text{Sm}^{3+}$  along

with smaller neighboring peaks assigned to the vibronic transitions of the mentioned main emission lines. The optimal concentration of  $\text{Sm}^{3+}$  is 0.3% (Figure 2c).

Although the XRD results (Figure 1b) suggest that the  $\text{Sm}^{3+}$  substitutes predominantly  $\text{Mg}^{2+}$  in the structure, one can identify the two-site emission of  $\text{Sm}^{3+}$  in the emission spectra of the sample with 0.1%  $\text{Sm}^{3+}$  by comparing the relative intensity of the maxima at 597 nm and 642.6 nm; the sample with 0.1%  $\text{Sm}^{3+}$  visibly exhibit stronger 597 nm emission as compared to other  $\text{Sm}^{3+}$  concentrations. This suggests that, in this sample, the  $\text{Sm}^{3+}$  ions are located in both  $\text{Mg}^{2+}$  and  $\text{Ba}^{2+}$  sites. For higher concentrations, as the lattice constant increases the  $\text{Ba}^{2+}$  site becomes less preferable for  $\text{Sm}^{3+}$  dopant, and as a result the emission becomes more uniform and seemingly one-site. The ratio between the orange and red emission is known to indicate the symmetry of the  $\text{Sm}^{3+}$  ions site; however, it is usually inferred that the red emission at 642.6 nm resulting from the electric-dipole (ED) type  ${}^4\text{G}_{5/2} \rightarrow {}^6\text{H}_{9/2}$  transition is dominant at low-symmetry sites [24], and orange emission at  $\sim 600$  nm resulting from the mixed electric-dipole/magnetic-dipole (ED + MD) type  ${}^4\text{G}_{5/2} \rightarrow {}^6\text{H}_{7/2}$  transition is dominant at high-symmetry octahedral sites [25]. This straightforward causation is, however, contested by the results of some highly-symmetrical double-perovskite materials such as  $\text{Ba}_2\text{ZnWO}_6:\text{Sm}^{3+}$ , which exhibits dominant red emission [26] similar to  $\text{BMM}:\text{Sm}^{3+}$ , as well as comparative studies between orthorhombic  $\text{LiCaBO}_3:\text{Sm}^{3+}$  and cubic  $\text{CsCaBO}_3:\text{Sm}^{3+}$  [27]. In the latter, the  $\text{Sm}^{3+}$  ions exhibit dominant red emission when located in octahedral sites of  $\text{CsCaBO}_3$  [28] and dominant orange emission when located in 7-coordinated sites in  $\text{LiCaBO}_3$  [29].  $\text{BMM}:\text{Sm}^{3+}$  is to our best knowledge the most clear example of dominant red emission of  $\text{Sm}^{3+}$  resulting from the location of the dopant in octahedral sites of high-symmetry cubic structures.

The excitation spectrum of  $\text{BMM}:\text{Sm}^{3+}$  monitored at the maximum intensity at 642 nm (Figure 3a) consists of broad bands in the UV/blue spectral region 300–450 nm, which originates from the absorption of the  $\text{O}^{2-} \rightarrow \text{Mo}^{6+}$  charge transfer. The excitation spectrum monitored at the maximum of the emission of the  $\text{Sm}^{3+}$  at the second (Ba) site consists of an additional band with maximum at 260 nm, which is due to excitation into Ba states in the conduction band [9]. In the visible part of the excitation spectrum, there are weaker lines associated with the  $4f-4f$  transitions labeled in the graph. Based on the complimentary data from the excitation, absorption, and emission spectra, the positions of the barycenter of  $\text{Sm}^{3+}$  energy levels were determined and listed in Table 1.

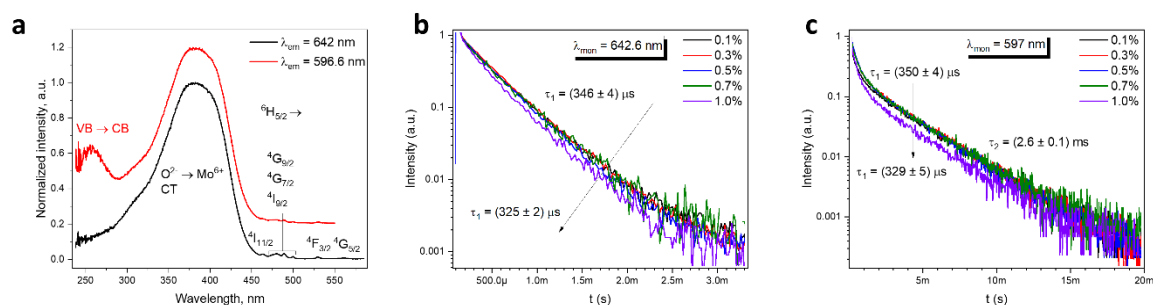


**Figure 3.** (a) Excitation spectra of the  $\text{BMM}:\text{Sm}^{3+}$  and (b,c) decay times of the  $\text{BMM}$  doped with  $\text{Sm}^{3+}$  monitored at 642.6 nm (b) and 597 nm (c).

The decay curves have two components: a short one and a long one (Figure 3b,c), which confirm the two-site emission of  $\text{Sm}^{3+}$ . The short component has a decay time around 350  $\mu\text{s}$  (Figure 3b). Such short decay times for  $\text{Sm}^{3+}$  luminescence have been observed in materials where  $\text{Sm}^{3+}$  is located at octahedral sites:  $\text{CaNb}_2\text{O}_6$  [30] and  $\text{TiO}_2$  [31]. The decay times become increasingly shorter when the dopant concentration increases, due to concentration quenching [32]. The long component is, as expected, more dominant in decay curves monitored at 597 nm (Figure 3c), and exhibit decay time  $2.6 \pm 0.2$  ms, observed commonly for  $\text{Sm}^{3+}$ -doped materials with a site coordination number other than 6, such as  $\text{SrAl}_4\text{O}_7$  [33] and  $\text{Sr}_2\text{SiO}_4$  [34].

**Table 1.** Barycenters of energy levels of  $\text{Sm}^{3+}$  in BMM host determined from the excitation ( $^4\text{I}_{11/2}, \dots, ^4\text{G}_{5/2}$ ), absorption ( $^6\text{F}_{11/2}, \dots, ^6\text{F}_{1/2}$ ), and emission spectra ( $^6\text{H}_{13/2}, \dots, ^6\text{H}_{7/2}$ ).

Level	Wavenumber ( $\text{cm}^{-1}$ )
$^4\text{I}_{11/2}$	21,575
$^4\text{G}_{9/2}$	20,812
$^4\text{G}_{7/2}$	20,429
$^4\text{I}_{9/2}$	20,008
$^4\text{F}_{3/2}$	18,879
$^4\text{G}_{5/2}$	17,857
$^6\text{F}_{11/2}$	10,520
$^6\text{F}_{9/2}$	9163
$^6\text{F}_{7/2}$	7999
$^6\text{F}_{5/2}$	7129
$^6\text{F}_{3/2}$	6634
$^6\text{H}_{15/2}$	6492
$^6\text{F}_{1/2}$	6380
$^6\text{H}_{13/2}$	5076
$^6\text{H}_{11/2}$	3663
$^6\text{H}_{9/2}$	2302
$^6\text{H}_{7/2}$	1095
$^6\text{H}_{5/2}$	0

The emission spectra of  $\text{BMM}:\text{Sm}^{3+}$  measured in the  $-193$ – $150$  °C range (Figure 4a) reveal that both the intensity and shape of the  $\text{Sm}^{3+}$  emission is strongly temperature-dependent. The thermal quenching of the emission intensity (Figure 4b) has two components when fitted with an Arrhenius equation (Figure S2) with corresponding activation energies of  $417$   $\text{cm}^{-1}$  and  $2054$   $\text{cm}^{-1}$ . The former component with smaller activation energy is absent, when the sample is excited at  $266$  nm into the Ba states (which constitute the conduction band); therefore, it is concluded that it must be associated with the quenching of the molybdate group charge transfer state. This is depicted in Figure 4c as a crossing between the ground state and the excited state parabolas. Similarly, low activation energy of thermal quenching was observed for the pure BMM host and  $\text{Eu}^{3+}$ -doped BMM [9]. The latter and larger activation energy can be matched with the thermalization of the  $^4\text{G}_{7/2}$  state, which may be involved in two-way energy transfer between the  $\text{Sm}^{3+}$  and  $\text{MoO}_6$  group, responsible for both  $\text{Sm}^{3+}$  emission and thermal quenching.

The shape of the emission spectra at a low temperature ( $77$  K) differs significantly from the room-temperature emission spectra (Figure 4d). The most dominant lines at  $77$  K cannot be assigned directly to the  $^4\text{G}_{5/2} \rightarrow ^6\text{H}_j$  transitions, but are noticeably distant from the room-temperature emission lines by the same wavenumbers, which correspond to the phonon energies derived from the Raman spectrum (Figure 1e). This is uncommon for  $\text{Sm}^{3+}$  emission at low temperature, which usually features  $^4\text{G}_{5/2} \rightarrow ^6\text{H}_j$  transitions unaccompanied by their phonon-related components [35]. Apparently due to the high symmetry of the BMM structure, the  $^4\text{G}_{5/2} \rightarrow ^6\text{H}_j$  transitions are forbidden and must be coupled with phonons to occur. This causes the material to only exhibit anti-Stokes phonon-coupled transitions at low temperatures. When the temperature is higher, the lattice distortions allow for direct  $^6\text{H}_{5/2} \rightarrow ^6\text{F}_j$  transitions. This unique phenomenon, observed previously for only a handful of materials doped with transition metal ions, such as  $\text{Cr}^{3+}$  or  $\text{Mn}^{4+}$  [36,37], allow for very sensitive temperature sensing using the fluorescence intensity ration (FIR) between the phonon-coupled emission at  $612$  nm and regular  $^4\text{G}_{5/2} \rightarrow ^6\text{H}_{9/2}$  emission at  $642$  nm (Figure 4e). The relative sensitivity calculated [38] from this FIR has a maximum of  $2.7\%$   $\text{K}^{-1}$  at  $-30$  °C and another local maximum of  $1.6\%$   $\text{K}^{-1}$  at  $75$  °C. Such a value is, to the best of our knowledge, one of the highest achieved for luminescent thermometry performed using only  $\text{Sm}^{3+}$  ions—comparable only to  $3.83\%$   $\text{K}^{-1}$  obtained in  $\text{Cs}_4\text{PbBr}_6$  borogermanate glass [39]—and significantly higher than, e.g.,  $0.5\%$   $\text{K}^{-1}$  for

YAG [40] and 0.26%  $K^{-1}$  for  $Ba_2Mg(PO_4)_2$  [41]. Higher sensitivities were obtained only for materials exhibiting Sm-independent host emission, e.g., 7.08%  $K^{-1}$  in  $CaWO_4$  [42] or 10.14%  $K^{-1}$  for  $TiO_2$  nanoparticles [43]. The obtained result, resulting purely from the high symmetry of the BMM host, sets a promising precedent for temperature sensing using high-symmetry perovskite materials.

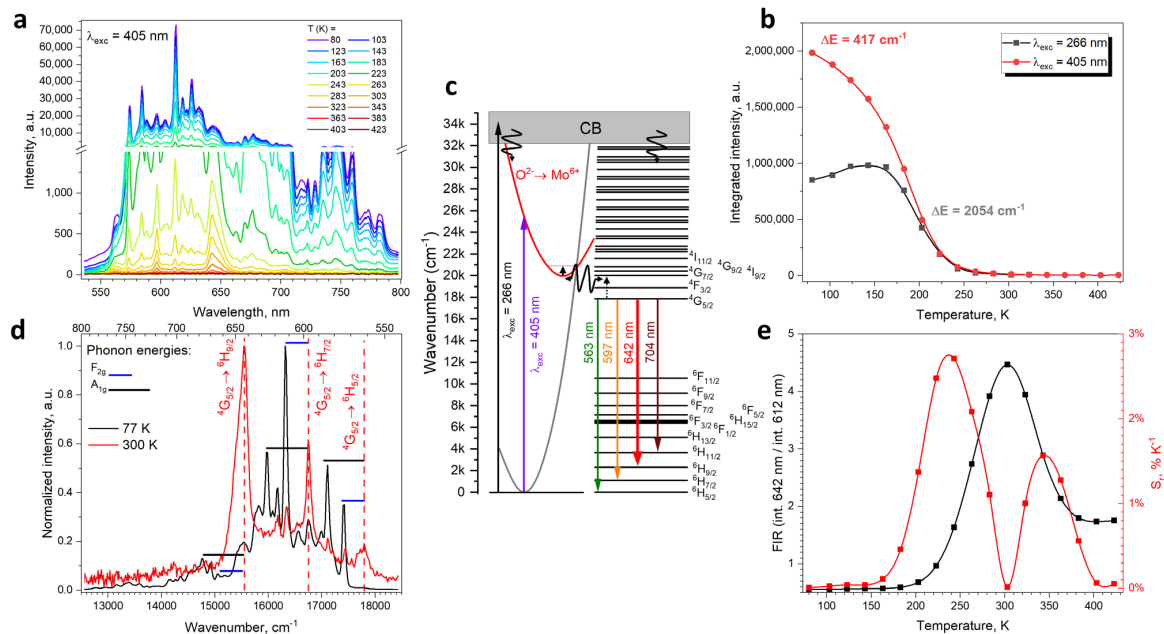


**Figure 4.** (a) Temperature-dependent emission spectra of BMM:0.3%  $Sm^{3+}$ , (b) thermal quenching curves, and corresponding activation energies of BMM:Sm $^{3+}$  under 405 and 266 nm excitation, (c) energy level scheme of the luminescent centers in  $Sm^{3+}$ -doped BMM, (d) 77 K and 300 K emission spectra of BMM:Sm $^{3+}$ , (e) FIR and relative sensitivity of temperature sensing.

The emission spectra with dominant red emission results in CIE color coordinates located at (0.631, 0.370) (Figure 5a). Such color coordinates located towards the red part of the color coordinate scale, work efficiently in lowering the CCT and enhancing the CRI of the commonly used cool white LEDs. To demonstrate the impact of BMM:Sm emission on the luminescence of the wLED, its spectrum was added to the spectrum of the commonly used wLED with CRI equal 85 and CCT equal 4059 K. The result is a white emission with CRI of 91 and CCT of 2943 K constituting the warm white emission (Figure 5b).

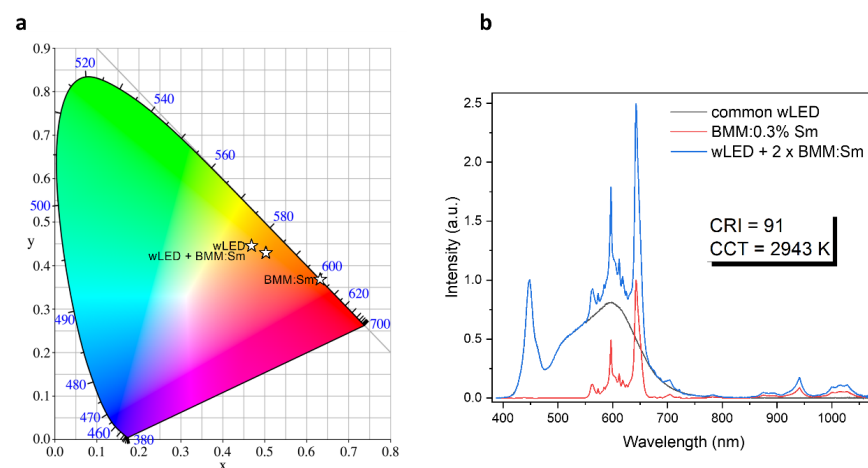


**Figure 5.** (a) CIE diagram of the BMM:0.3%  $Sm^{3+}$ , (b) normalized emission spectra of common wLED, BMM doped with  $Sm^{3+}$ , and simulated luminescence of combined wLED and BMM:Sm $^{3+}$ .

### 3. Conclusions

Molybdates with a double-perovskite structure with the formula  $\text{Ba}_2\text{MgMoO}_6$  doped with  $\text{Sm}^{3+}$  ions were successfully obtained for the first time using the co-precipitation method. The electric dipole (ED)  $^4\text{G}_{5/2} \rightarrow ^6\text{H}_{9/2}$  transition dominates; although, the  $\text{Sm}^{3+}$  ions are located in high symmetry, and the spectroscopic properties are characteristic for  $\text{Sm}^{3+}$  at octahedral sites with 6-fold coordination. Two-site  $\text{Sm}^{3+}$  emission was identified in the emission spectra of the 0.1%  $\text{Sm}^{3+}$  sample by comparing the relative intensity of the maxima at 597 nm and 642.6 nm. The obtained results suggest that in this sample  $\text{Sm}^{3+}$  ions are located in both  $\text{Mg}^{2+}$  and  $\text{Ba}^{2+}$  sites. At higher concentrations, the  $\text{Ba}^{2+}$  site is less preferable for  $\text{Sm}^{3+}$  doping, and as a result, the emission becomes more uniform and single-site. The aim of our work was to improve the properties of white-light-emitting diode lighting by supplying the missing red component and optimizing its correlated color temperature and color-rendering index. We can successfully conclude that the obtained BMM: $\text{Sm}^{3+}$  materials are good candidates as a red phosphor, achieving a simulated CRI value of 91 and a CCT of 2943 K, giving a warm white emission. Temperature measurements brought us completely unexpected results. The relative sensitivity calculated from FIR is a maximum of  $2.7\% \text{ K}^{-1}$  at  $-30^\circ\text{C}$  and another local maximum of  $1.6\% \text{ K}^{-1}$  at  $75^\circ\text{C}$ . This value is one of the highest achieved for luminescence thermometry performed only using  $\text{Sm}^{3+}$  ions. This is an extremely promising precedent for temperature sensing using perovskite materials with high symmetry that results from the high symmetry of the BMM host.

**Supplementary Materials:** The following supporting information can be downloaded at: <https://www.mdpi.com/article/10.3390/ma17081897/s1>, Figure S1: Histogram of the average crystal size; Figure S2: Fitting of an Arrhenius equation to temperature-dependent emission intensity of BMM:  $\text{Sm}^{3+}$  excited at 405 nm (left) and 266 nm (right).

**Author Contributions:** Conceptualization, N.M.-G.; Methodology, N.M.-G.; Formal analysis, N.M.-G. and B.B.; Investigation, N.M.-G.; Data curation, N.M.-G., B.B. and M.P.; Writing—original draft, N.M.-G. and B.B.; Writing—review & editing, N.M.-G. and B.B.; Supervision, P.J.D.; Project administration, N.M.-G. and P.J.D. All authors have read and agreed to the published version of the manuscript.

**Funding:** This research received no external funding.

**Institutional Review Board Statement:** Not applicable.

**Informed Consent Statement:** Not applicable.

**Data Availability Statement:** No new data were created or analyzed in this study. Data sharing is not applicable to this article.

**Acknowledgments:** The authors acknowledge support by a statutory activity subsidy from the Polish Ministry of Science and Higher Education for the Institute of Low Temperature and Structure Research Polish Academy of Sciences.

**Conflicts of Interest:** The authors declare no conflict of interest.

### References

1. Shkerin, S.N.; Uporov, S.A.; Yudin, V.N.; Solodovnikov, S.F.; Zolotova, E.S.; Tolkacheva, A.S. Paramagnetic properties of triple molybdates  $\text{CsNa}_5\text{M}_3(\text{MoO}_4)_6$  ( $\text{M} = \text{Ni}, \text{Co}, \text{Mn}$ ). *Russ. J. Phys. Chem. A* **2016**, *90*, 2292–2296. [CrossRef]
2. Soltys, E.V.; Urazov, K.; Kharlamova, T.S.; Vodyankina, O.V. Redox and Catalytic Properties of Copper Molybdates with Various Composition. *Kinet. Catal.* **2018**, *59*, 58–69. [CrossRef]
3. Soficha, D.; Tushinova, Y.L.; Shendrik, R.; Bazarov, B.G.; Dorzhieva, S.G.; Chimitova, O.D.; Bazarova, J.G. Optical spectroscopy of molybdates with composition  $\text{Ln}_2\text{Zr}_3(\text{MoO}_4)_9$  ( $\text{Ln}: \text{Eu}, \text{Tb}$ ). *Opt. Mater.* **2018**, *81*, 71–77. [CrossRef]
4. Sofich, D.O.; Dorzhieva, S.G.; Chimitova, O.D.; Bazarov, B.G.; Tushinova, Y.L.; Bazarova, Z.G.; Shendrik, R.Y. Hypersensitive  $^5\text{D}_0\text{-}^7\text{F}_2$  Transition of Trivalent Europium in Double Molybdates. *Bull. Russ. Acad.* **2019**, *83*, 321–323. [CrossRef]
5. Nagamani Naidu, B.; Koteswara Rao, K.; Murali Krishna, M.P.S. Sol-gel synthesis, crystal structure and luminescence properties of  $\text{Eu}^{3+}$  doped double perovskite molybdates  $\text{NaCaBi}_{1-x}\text{Eu}_x\text{MoO}_6$  ( $x = 0\text{-}0.27$ ). *Mater. Res. Express.* **2019**, *6*, 116210. [CrossRef]

6. Takeda, T.; Ito, M.; Kikkawa, S. Preparation of magneto-resistive  $\text{Sr}_2\text{FeMoO}_6$  through molybdic acid gelation. *J. Alloys Compd.* **2008**, *449*, 93–95. [[CrossRef](#)]
7. Rath, M.K.; Lee, K.-T. Characterization of novel  $\text{Ba}_2\text{LnMoO}_6$  (Ln = Pr and Nd) double perovskite as the anode material for hydrocarbon-fueled solid oxide fuel cells. *J. Alloys Compd.* **2018**, *737*, 152–159. [[CrossRef](#)]
8. Chan, W.-L.; Liu, Z.; Lu, S.; Tanner, P.A.; Wong, K.-L. The reported anomalous emission intensity of the  $^5\text{D}_0 \rightarrow ^7\text{F}_4$  transition of  $\text{Eu}^{3+}$  in a molybdate double perovskite. *J. Mater. Chem. C* **2015**, *3*, 860–963. [[CrossRef](#)]
9. Bondzior, B.; Stefańska, D.; Vu, T.H.Q.; Dereń, P.J. Optimization of  $\text{Eu}^{3+}$ -to-Host Emission Ratio in Double-Perovskite Molybdenites for Highly Sensitive Temperature Sensors. *J. Phys. Chem. C* **2022**, *126*, 13247–13255. [[CrossRef](#)]
10. Krishnan, R.; Kroon, R.E.; Swart, H.C. Charge transfer characteristics and luminescence properties of  $\text{Eu}^{3+}$  activated  $\text{Ba}_2\text{YMoO}_6$  and  $\text{BaY}_2(\text{MoO}_4)_4$  phosphors. *Mater. Res. Bull.* **2022**, *145*, 111554. [[CrossRef](#)]
11. Zhang, S.; Hu, Y.; Chen, L.; Wang, X.; Ju, G.; Fan, Y. A novel  $\text{Ba}_2\text{MgMoO}_6:\text{Eu}^{3+}$  orange-red phosphor: Photoluminescence properties and mechanism of charge and energy transfer. *J. Mater. Res.* **2013**, *28*, 3130–3136. [[CrossRef](#)]
12. Zhang, L.; Sun, B.; Shao, C.; Zhen, F.; Wei, S.; Bu, W.; Yao, Q.; Jiang, Z.; Chen, H. Preparation, band-structure and luminescence of double perovskite  $\text{Ba}_2\text{MgMoO}_6:\text{Eu}^{3+}$  orange-red phosphor for white LEDs. *Ceram. Int.* **2018**, *44*, 17305–17312. [[CrossRef](#)]
13. Wang, Y.; Ke, Y.; Chen, S.; Luo, J.; Shu, S.; Gao, J.; Deng, B.; Yu, R. Luminescence investigation of red-emitting  $\text{Sr}_2\text{MgMoO}_6:\text{Eu}^{3+}$  phosphor for visualization of latent fingerprint. *J. Colloid Interface Sci.* **2021**, *583*, 89–99. [[CrossRef](#)] [[PubMed](#)]
14. Cao, R.; Huang, T.; Nie, J.; Zhang, L.; Chen, Y.; Li, L.; Lan, B.; Wang, J. Energy transfer and tunable-color luminescence properties of a single-phase  $\text{CaSrNb}_2\text{O}_7:\text{Sm}^{3+}; \text{Bi}^{3+}$ . *J. Mol. Struct.* **2024**, *1297*, 136962. [[CrossRef](#)]
15. Cao, R.; Wei, J.; Chen, T.; Lan, B.; Li, L.; Liu, R.; Luo, Z.; Wang, J. Synthesis, adjustable-color emission and energy transfer of  $\text{Ba}_2\text{MgSi}_2\text{O}_7: \text{Sm}^{3+}, \text{Bi}^{3+}$  phosphor. *J. Mol. Struct.* **2023**, *1274*, 134404. [[CrossRef](#)]
16. Stefańska, D.; Bondzior, B.; Vu, T.H.Q.; Miniajluk-Gaweł, N.; Dereń, P.J. The Influence of Morphology and  $\text{Eu}^{3+}$  Concentration on Luminescence and Temperature Sensing Behavior of  $\text{Ba}_2\text{MgWO}_6$  Double Perovskite as a Potential Optical Thermometer. *J. Alloys Compd.* **2020**, *842*, 155742. [[CrossRef](#)]
17. Yan, L.; Xing, M.; Ma, Y.; Kang, L.; Fu, Y.; Pang, Q.; Xin, F.; Wang, H.; Luo, X. Promising lanthanide-doped double molybdates  $\text{KYb}(\text{MoO}_4)_2$  phosphor for highly efficient upconversion luminescence and temperature sensing. *Spectrochim. Acta A Mol. Biomol. Spectrosc.* **2024**, *308*, 123751. [[CrossRef](#)] [[PubMed](#)]
18. Chen, H.; Jin, Y.; Fang, F.; Lin, H.; Li, Y.; Feng, G.; Xiong, Y.; Meng, F.; Cao, L.; Ren, H. Up-conversion phosphor  $\text{Na}_2\text{MoO}_4:\text{Er}^{3+}/\text{Yb}^{3+}$  for the optical temperature sensing and anticounterfeiting. *J. Lumin.* **2024**, *265*, 120244. [[CrossRef](#)]
19. Tian, X.; Xu, S.; Wen, J.; Zhu, L.; Ji, C.; Huang, Z.; Wang, X.; Luo, F.; Liu, X.; Lu, Y.; et al. Thermochromic  $\text{Pr}^{3+}$  doped  $\text{CaMoO}_4$  phosphor with diverse thermal responses for temperature sensing. *Ceram. Int.* **2023**, *49*, 27126–27137. [[CrossRef](#)]
20. Armaroli, N.; Bolink, H.J. Photoluminescent Materials and Electroluminescent Devices. In *Topics in Current Chemistry Collections*; Springer: Berlin/Heidelberg, Germany, 2017. [[CrossRef](#)]
21. Ye, S.; Wang, C.-H.; Jing, X.-P. Photoluminescence and Raman Spectra of Double-Perovskite  $\text{Sr}_2\text{Ca}(\text{Mo}/\text{W})\text{O}_6$  with A- and B-Site Substitutions of  $\text{Eu}^{3+}$ . *J. Electrochem. Soc.* **2008**, *155*, 148. [[CrossRef](#)]
22. Pásztorová, J.; Bi, W.H.; Gaal, R.; Krämer, K.; Živković, I.; Rønnow, H.M. Structure, heat capacity and Raman spectra of  $\text{Ba}_2\text{MgWO}_6$  single crystals grown in  $\text{BaCl}_2\text{-MgCl}_2$  flux. *J. Solid State Chem.* **2023**, *326*, 124184. [[CrossRef](#)]
23. Fujioka, Y.; Frantti, J.; Kakihana, M. Raman Scattering Studies of the  $\text{Ba}_2\text{MnWO}_6$  and  $\text{Sr}_2\text{MnWO}_6$  Double Perovskites. *J. Phys. Chem. B* **2006**, *110*, 777–783. [[CrossRef](#)]
24. Görller-Walrand, C.; Binnemans, K. Chapter 167 Spectral Intensities of f-f Transitions. In *Handbook on the Physics and Chemistry of Rare Earths*; Elsevier: Amsterdam, The Netherlands, 1998; Volume 25, pp. 101–264.
25. Shih, H.-R.; Chang, Y.-S. Structure and Photoluminescence Properties of  $\text{Sm}^{3+}$  Ion-Doped  $\text{YInGe}_2\text{O}_7$  Phosphor. *Materials* **2017**, *10*, 779. [[CrossRef](#)]
26. Chen, P.; Hu, W.; Yang, D.; Zhu, J.; Zhang, J.; Wu, Y.  $\text{Ba}_2\text{ZnWO}_6:\text{Sm}^{3+}$  as promising orange-red emitting phosphors: Photoluminescence properties and energy transfer process. *Phys. B Condens.* **2018**, *530*, 127–132. [[CrossRef](#)]
27. Herrmann, A.; Friedrich, D.; Zschechel, T.; Rüssel, C. Luminescence properties of  $\text{Sm}^{3+}$  doped alkali/earth alkali orthoborates of the type  $\text{XZBO}_3$  with X = Li, Na, Cs and Z = Ca, Sr, Ba. *J. Lumin.* **2019**, *214*, 116550. [[CrossRef](#)]
28. Wen, M.; Wu, H.; Su, X.; Lu, J.; Yang, Z.; Wu, X.; Pan, S.  $\text{ACaBO}_3$  (A = Cs, Rb): Two new cubic borates with isolated  $\text{BO}_3$  groups. *Dalton Trans.* **2017**, *46*, 4968–4974. [[CrossRef](#)] [[PubMed](#)]
29. Wu, L.; Chen, X.L.; Li, H.; He, M.; Dai, L.; Li, X.Z.; Xu, Y.P. Structure determination of a new compound  $\text{LiCaBO}_3$ . *J. Solid State Chem.* **2004**, *177*, 1111–1116. [[CrossRef](#)]
30. Li, K.; Liu, X.; Zhang, Y.; Li, X.; Lian, H.; Lin, J. Host-Sensitized Luminescence Properties in  $\text{CaNb}_2\text{O}_6:\text{Ln}^{3+}$  ( $\text{Ln}^{3+} = \text{Eu}^{3+}/\text{Tb}^{3+}/\text{Dy}^{3+}/\text{Sm}^{3+}$ ) Phosphors with Abundant Colors. *Inorg. Chem.* **2015**, *54*, 323–333. [[CrossRef](#)]
31. Luo, W.; Li, R.; Chen, X. Host-Sensitized Luminescence of  $\text{Nd}^{3+}$  and  $\text{Sm}^{3+}$  Ions Incorporated in Anatase Titania Nanocrystals. *J. Phys. Chem. C* **2009**, *113*, 8772–8777. [[CrossRef](#)]
32. Timoshenko, A.D.; Matvienko, O.O.; Doroshenko, A.G.; Parkhomenko, S.V.; Vorona, I.O.; Kryzhanovska, O.S.; Safronova, N.A.; Vovk, O.O.; Tolmachev, A.V.; Baumer, V.N.; et al. Highly-doped  $\text{YAG}:\text{Sm}^{3+}$  transparent ceramics: Effect of  $\text{Sm}^{3+}$  ions concentration. *Ceram. Int.* **2023**, *49*, 7524–7533. [[CrossRef](#)]
33. Puchalska, M.; Zych, E. The effect of charge compensation through alkali metal co-doping on the luminescence behaviour of  $\text{SrAl}_4\text{O}_7:\text{Sm}^{3+}$  phosphor. *J. Lumin.* **2018**, *197*, 211–218. [[CrossRef](#)]

34. Gupta, S.K.; Pathak, N.; Thulasidas, S.K.; Natarajan, V. Local site symmetry of  $\text{Sm}^{3+}$  in sol–gel derived  $\alpha'$ - $\text{Sr}_2\text{SiO}_4$ : Probed by emission and fluorescence lifetime spectroscopy. *J. Lumin.* **2016**, *169*, 669–673. [[CrossRef](#)]
35. Solarz, P.; Dominika-Dzik, G.; Lisiecki, R.; Ryba-Romanowski, W.; Beregi, E.; Foldvari, I.; Lengyel, K. Spectroscopic properties of  $\text{Sm}^{3+}$  impurity in  $\text{YAl}_3(\text{BO}_3)_4$  single crystal. *Opt. Mater.* **2010**, *32*, 1446–1450. [[CrossRef](#)]
36. Li, R.; Li, P.; Wei, G.; Li, J.; Shi, Y.; Wang, Y.; He, S.; Yang, Y.; Ding, W.; Wang, Z. Ultra-sensitive low-temperature thermometer regulated by the crystal field strength. *Ceram. Int.* **2023**, *49*, 7913–7919. [[CrossRef](#)]
37. Cai, P.; Wang, X.; Seo, H.J. Excitation power dependent optical temperature behaviors in  $\text{Mn}^{4+}$  doped oxyfluoride  $\text{Na}_2\text{WO}_2\text{F}_4$ . *Phys. Chem. Chem. Phys.* **2018**, *20*, 2028–2035. [[CrossRef](#)]
38. Brites, C.D.S.; Millán, A.; Carlos, L.D. Chapter 281—Lanthanides in Luminescent Thermometry. In *Handbook on the Physics and Chemistry of Rare Earths*; Elsevier: Amsterdam, The Netherlands, 2016; Volume 49, pp. 339–427.
39. Yao, G.; Li, S.; Valiev, D.; Chen, M.; Stepanow, S.; Lu, Y.; Li, C.; Zhou, Y.; Su, Z.; Zeng, F. Luminescence behavior and temperature sensing properties of  $\text{Sm}^{3+}$ -doped  $\text{Cs}_4\text{PbBr}_6$  quantum dots encapsulated in borogermanate glass. *J. Non-Cryst. Solids* **2022**, *582*, 121462. [[CrossRef](#)]
40. Zhu, K.; Zhou, H.; Qiu, J.; Wang, L.-G.; Ye, L. Optical temperature sensing characteristics of  $\text{Sm}^{3+}$  doped YAG single crystal fiber based on luminescence emission. *J. Alloys Compd.* **2022**, *890*, 161844. [[CrossRef](#)]
41. Singn, R.; Bedyyal, A.K.; Manhas, M.; Durani, F.; Swart, H.C.; Kumar, V. Effect of the synthesis route on luminescence dynamics and thermographic properties of  $\text{Sm}^{3+}$  doped  $\text{Ba}_2\text{Mg}(\text{PO}_4)_2$  phosphor. *J. Alloys Compd.* **2024**, *973*, 172911. [[CrossRef](#)]
42. Lan, Q.; Meng, Q. Temperature sensing materials based on the FIR of doped ions and the matrix in  $\text{CaWO}_4:\text{Sm}^{3+}$  phosphors. *Sens. Actuator A-Phys.* **2023**, *363*, 114708. [[CrossRef](#)]
43. Dramićanin, M.D.; Antić, Ž.; Čulubrk, S.; Ahrenkiel, S.P.; Nedeljković, J.M. Self-referenced luminescence thermometry with  $\text{Sm}^{3+}$  doped  $\text{TiO}_2$  nanoparticles. *Nanotechnology* **2014**, *25*, 485501. [[CrossRef](#)]

**Disclaimer/Publisher’s Note:** The statements, opinions and data contained in all publications are solely those of the individual author(s) and contributor(s) and not of MDPI and/or the editor(s). MDPI and/or the editor(s) disclaim responsibility for any injury to people or property resulting from any ideas, methods, instructions or products referred to in the content.